CHEMISTRY OF MATERIALS

Article

pubs.acs.org/cm

Fast Lithium Ion Conduction in Li_2SnS_3: Synthesis, Physicochemical Characterization, and Electronic Structure

Jacilynn A. Brant,[†] Danielle M. Massi,[†] N. A. W. Holzwarth,[‡] Joseph H. MacNeil,[#] Alexios P. Douvalis,[∥] Thomas Bakas,[∥] Steve W. Martin,[⊥] Michael D. Gross,[§] and Jennifer A. Aitken*[,†]

[†]Department of Chemistry and Biochemistry, Duquesne University, Pittsburgh, Pennsylvania 15282, United States

[‡]Department of Physics, [§]Department of Chemistry, Wake Forest University, Winston-Salem, North Carolina 27109, United States

[∥]Department of Physics, University of Ioannina, Ioannina 45110, Greece

[⊥]Department of Materials Science and Engineering, Iowa State University, Ames, Iowa 50011 United States

[#]Department of Chemistry, Chatham University, Pittsburgh, Pennsylvania 15232, United States

Supporting Information

ABSTRACT: Li_2SnS_3 is a fast Li^+ ion conductor that exhibits high thermal stability (mp ~750 °C) as well as environmental stability under ambient conditions. Polycrystalline Li_2SnS_3 was synthesized using high-temperature, solid-state synthesis. According to single-crystal X-ray diffraction, Li_2SnS_3 has a sodium chloride-like structure (space group $C2/c$), a result supported by synchrotron X-ray powder diffraction and ^{119}Sn Mössbauer spectroscopy. According to impedance spectroscopy, Li_2SnS_3 exhibits Li^+ ion conductivity up to 1.6×10^{-3} S/cm at 100 °C, which is among the highest for ternary chalcogenides. First-principles simulations of Li_2SnS_3 and the oxide analogue, Li_2SnO_3, provide insight into the basic properties and mechanisms of the ionic conduction. The high thermal stability, significant lithium ion conductivity, and environmental stability make Li_2SnS_3 a promising new solid-state electrolyte for lithium ion batteries.

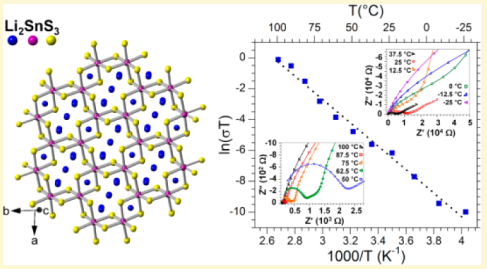

1. INTRODUCTION

To advance the next generation of batteries, there is a movement toward nonflammable solid electrolytes as a replacement for organic liquid electrolytes. While the safety advantages of solid-state ionics are widely acknowledged, chemical, electrochemical, and environmental stabilities as well as ionic conductivities must be optimized for practical applications. Lithium superionic conductors, which exhibit rapid diffusion of lithium ions through the lattice well below the melting temperature,[1] are relatively scarce.

An assortment of materials, including polymers, glasses, crystals, and others, have been explored toward the discovery of superionic conductors.[1,2] However, Li_3N has been difficult to surpass until recently. Li_3N has high ion conductivity, $\sigma_{300°C} = 1.2 \times 10^{-3}$ S/cm and $\sigma_{25°C} = 1.2 \times 10^{-4}$ S/cm perpendicular to the crystallographic c axis,[2a] but it has been plagued by a low electrochemical decomposition potential. The search for improved properties has resulted in enhanced materials at the forefront of solid-state ionics, including polymer electrolytes such as lithium complexes of poly(ethylene oxide) ($\sigma_{25°C} \sim 10^{-5}$ S/cm),[2b,c] glassy materials such as $Li_2S-SiS_2-Li_3PO_4$ ($\sigma_{25°C} \sim 10^{-4}$ S/cm),[2d,e] glassy ceramics such as $Li_2S:P_2S_5$ ($\sigma_{25°C} \sim 10^{-3}-10^{-5}$ S/cm), and crystalline oxide perovskites such as $La_{0.5}Li_{0.5}TiO_3$ ($\sigma_{25\ °C} \sim 10^{-3}$ to 10^{-5} S/cm).[2f−h] Lithium super ion conductors (LISICONs), e.g., $Li_{2+2x}Zn_{1-x}GeO_4$ with $\sigma_{25°C} = 1 \times 10^{-7}$ S/cm,[2i,j] have been improved upon by incorporating chalcogenides to form thio-LISICONs with superior room-temperature ion conductivities on the order of 10^{-5} to 10^{-9} S/cm, e.g., $Li_{4+x+\delta}(Ge_{1-\delta'-x}\text{-}Ga_x)S_4$ and $Li_{4-2x}Zn_xGeS_4$.[2k] Further development has led to replacing Zn with P, yielding $Li_{4-x}Ge_{1-x}P_xS_4$ that exhibits an ion conductivity of 2.2×10^{-3} S/cm at 25 °C.[2l]

Crystalline lithium sulfides are among the top contenders for use as solid-state electrolytes in batteries. In fact, the $Li_{10}GeP_2S_{12}$[1,3] solid exhibits a room-temperature ion conductivity of 10^{-2} S/cm, which is on par with organic liquid electrolytes.[4] Furthermore, it has demonstrated excellent performance in a battery with a $LiCoO_2/Li_{10}GeP_2S_{12}/In$ structure.[1] However, widespread use of $Li_{10}GeP_2S_{12}$ is limited by the relatively high cost of Ge. Accordingly, the quest for germanium-free lithium ion conductors has led to the development of $Li_{11}SiP_2S_{12}$,[5] which exhibits slightly higher Li^+ conductivity than the Ge-analogue; however, synthesis scalability is problematic, as it requires high pressures, and phase-purity has not been achieved. On the other hand, the synthesis of $Li_{10}SnP_2S_{12}$ is easily scalable.[6] Accordingly, $Li_{10}SnP_2S_{12}$ is commercially available as a superionic solid under the name NANOMYTE SSE-10, although it has a slightly lower conductivity than that of $Li_{10}GeP_2S_{12}$.[6] The appeal of $Li_{10}SnP_2S_{12}$ is also manifested by the wide window of

Received: October 12, 2014
Revised: December 3, 2014
Published: December 4, 2014

DOI: 10.1021/cm5037524
Chem. Mater. 2015, 27, 189−196

electrochemical stability that is comparable to that of $Li_{10}GeP_2S_{12}$.[1] Lithium sulfides constructed from cheap and earth-abundant elements have recently taken precedence in the pursuit of superionic conductors with suitable mechanical properties[7] as well as improved stabilities. In fact, it has recently been shown that aliovalent substitution in Li_4SnS_4 (i.e., $Li_{4-x}Sn_{1-x}As_xS_4$ where x = 0 to 0.25) has yielded an ion conductor with excellent air stability.[8] Interestingly, undoped ternary lithium sulfides have not yet been fully explored.

In this work, Li_2SnS_3 is presented as a fast lithium ion conductor with high thermal and air stabilities. A pristine polycrystalline powder of Li_2SnS_3 was prepared via solid-state synthesis. The structure of the sodium chloride-like Li_2SnS_3 (Figure 1) was characterized using single-crystal X-ray diffraction, synchrotron X-ray powder diffraction, and ^{119}Sn Mössbauer spectroscopy. First-principles simulations of Li_2SnS_3 are presented in comparison with the oxide analogue, Li_2SnO_3, in order to develop insight into the basic properties of the material, especially with respect to ion conductivity.

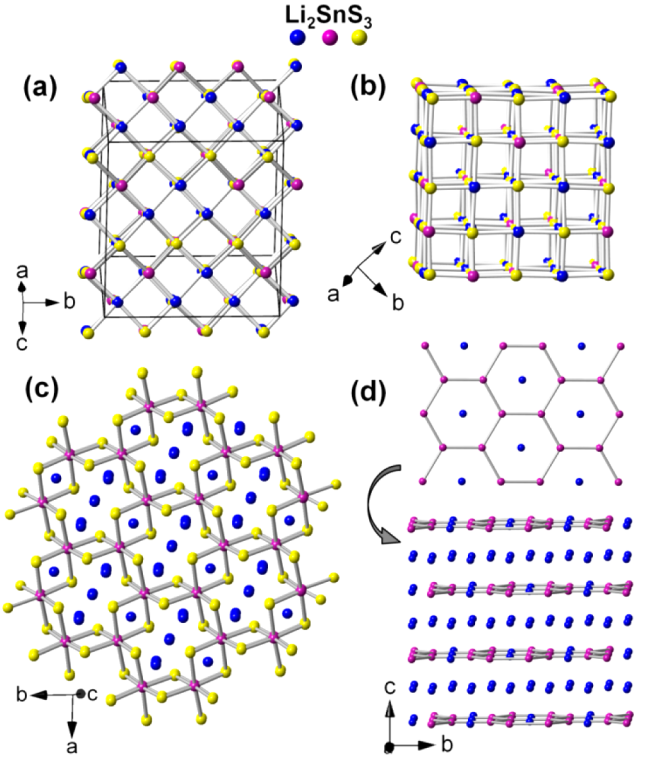

Figure 1. (a) One unit cell of the Li_2SnS_3 crystal structure. (b) Alternating octahedral cations and S^{2-} anions constitute a NaCl-like network. (c) Layers in the *ab* plane in which Li−S bonds have been removed to highlight the Sn−S framework. (d) Layers in the *ab* plane with S atoms removed to view the honeycomb-like arrangement of Sn atoms. Lines are drawn between Sn vertices to emphasize the net topology.

2. EXPERIMENTAL SECTION

2.1. Synthesis. All chemicals were used as obtained: lithium sulfide powder, ~200 mesh, 99.9%, Cerac Milwaukee, WI; tin powder, ~200 mesh, 99.99%, Cerac Milwaukee, WI; sulfur powder, sublimed, 99.5%, Fisher Scientific Pittsburgh, PA. Li_2SnS_3 was prepared by grinding stoichiometric amounts of Li_2S (1 mmol, 0.0460 g), Sn (1 mmol, 0.1187 g), and S (2 mmol, 0.0647 g) using an agate mortar and pestle in an argon-filled glovebox. Inside of a 12 mm o.d. fused-silica tube, the mixture was contained in a graphite crucible. The tube was sealed under a vacuum of ~10^{-3} mbar. The sample was heated at a rate of 50 °C/h to 750 °C and held at 750 °C for 96 h, slowly cooled to 500 °C in 125 h, and then allowed to cool to room temperature. The product is a dark-green polycrystalline powder, as observed under an optical microscope.

2.2. Sample Preparation. The Li_2SnS_3 sample was ground for 30 min in preparation for synchrotron X-ray powder diffraction (SXRPD), ^{119}Sn Mössbauer spectroscopy, differential thermal analysis, and diffuse reflectance UV−vis−NIR spectroscopy. In preparation for impedance spectroscopy, the ground sample was pelletized, with a diameter of 13 mm and a height of 1.24 mm, with a Carver press using 15 000 psi. The density of the pellet was determined to be ~56% of the theoretical density. The pellet was covered with a circular mask with a diameter of 9.9 mm in preparation for Au sputtering, which was performed with a Hummer 6.6 sputter coater in a N_2-filled glovebox.

2.3. Single-Crystal X-ray Diffraction. A Bruker SMART Apex 2 CCD single-crystal X-ray diffractometer using graphite monochromatized molybdenum K_α radiation (λ = 0.71073 Å) with a tube power of 50 kV and 30 mA was used to collect single-crystal diffraction data for a dark-green, block-like crystal of Li_2SnS_3 for 20 s per frame at room temperature. Over a hemisphere of data were collected in 0.3° steps in ω and ϕ. SAINT was used for data integration, and SADABS was used to apply the absorption correction.[9] XPREP was used for space group determination and to create files for SHELXTL.[10] Two space groups were initially considered based on systematic absences, *Cc* and *C2/c*. The centrosymmetric space group *C2/c* (#15) was selected due to the intensity statistics ($|E^2 - 1| = 1.041$).

The crystal structure of Li_2SnS_3 was solved and refined using the SHELXTL-PC software package.[11] The final refinement of Li_2SnS_3 yielded an R1(all data) of 1.75%. All atoms were refined anisotropically, with the exception of the isotropic refinement of Li(1). Crystallographic details are displayed in Table 1. Atomic coordinates and bond lengths are displayed in Tables S1−S3. All crystal structure figures were generated using CrystalMaker.

Table 1. Crystallographic Data and Experimental Details[a]

empirical formula	Li_2SnS_3
size	0.04 × 0.05 × 0.05 mm
temperature	298 K
wavelength of X-ray	0.71073 Å
space group	*C2/c*
unit cell dimensions	*a* = 6.3964(5) Å
	b = 11.0864(9) Å
	c = 12.405(1) Å
	β = 99.867(5)°
volume, *Z*	866.7(1) Å^3, 8
calculated density	3.507 g cm^{-3}
reflections collected/unique	5921/969
data/restraints/parameters	969/0/54
completeness to theta = 27.11°	100%
goodness of fit	1.06
final R indices [$I > 2\sigma(I)$]	R1 = 0.0131, wR_2 = 0.0286
R indices (all data)	R1 = 0.0174, wR_2 = 0.0302
highest peak, deepest hole	0.41 and −0.46 e/Å^3

[a]Refinement of F^2 was made against all reflections. $R_1 = (\sum||F_o| - |F_c||)/(\sum|F_o|)$, $wR_2 = (\sum[w(F_o^2 - F_c^2)^2]/\sum[w(F_o^2)^2])^{1/2}$, $w = 1/(\sigma^2(F_o^2) + (aF_o)^2 + bP)$, $P = [2F_c^2 + \max(F_o^2,0)]/3$

2.4. Synchrotron X-ray Powder Diffraction (SXRPD) and Rietveld Refinement. Room-temperature SXRPD data were collected at the Advanced Photon Source, Argonne National Laboratory, at the 11-BM line. The 11-BM instrument uses X-ray optics with two platinum-striped mirrors and a double-crystal Si(111) monochromator, where the second crystal has an adjustable sagittal bend.[12] Ion chambers monitor incident flux. A vertical Huber 480 goniometer, equipped with a Heidenhain encoder, positions an analyzer system composed of 12 perfect Si(111) analyzers and 12

DOI: 10.1021/cm5037524
Chem. Mater. 2015, 27, 189−196

Oxford-Danfysik $LaCl_3$ scintillators, with a spacing of 2° 2θ.[13] The analyzer orientation can be adjusted individually on two axes. A three-axis translation stage holds the sample mounting and allows it to be spun, typically at ~5400 rpm (90 Hz). A Mitsubishi robotic arm is used to mount and dismount samples on the diffractometer.

The diffractometer is controlled via EPICS.[14] Data are collected while continually scanning the diffractometer 2θ arm. A mixture of NIST standard reference materials, Si (SRM 640c) and Al_2O_3 (SRM 676), is used to calibrate the instrument, where the Si lattice constant determines the wavelength for each detector. Corrections are applied for detector sensitivity, 2θ offset, small differences in wavelength between detectors, and the source intensity, as noted by the ion chamber before merging the data into a single set of intensities evenly spaced in 2θ.

GSAS was used with the EXPGUI interface for Rietveld refinement.[15] The crystal structure of Li_2SnS_3 that was obtained in this work using single-crystal X-ray diffraction was used as the starting model. A shifted Chebyshev polynomial was used for background correction. Lorentzian isotropic crystallite size broadening (LX) and Lorentzian isotropic strain broadening (LY) terms within the type-3 profile function were used to model peak shapes. Lattice parameters, atomic coordinates, isotropic displacement parameters, and site occupation factors were refined.

2.5. ^{119}Sn Mössbauer Spectroscopy. A constant acceleration spectrometer equipped with a calcium stannate ($Ca^{119m}SnO_3$) source that is kept at room temperature was used for the collection of the ^{119}Sn Mössbauer spectrum on the powder Li_2SnS_3 sample. A Thor Cryogenics variable-temperature liquid nitrogen cryostat was used for the measurement at 80 K. The spectrometer was calibrated with metallic iron at room temperature. The spectrum analyses were performed with the use of a recently developed Mössbauer fitting program.[16]

2.6. Impedance Spectroscopy. A Novocontrol Technologies Concept 80 impedance spectrometer was used to collect complex impedance spectra for pressed pellets of Li_2SnS_3 at frequencies ranging from 1 Hz to 3 MHz with an applied root-mean-square ac voltage of 1 V. The Li_2SnS_3 pellet was held in a two-electrode, airtight sample holder that contains spring-loaded Pt mesh contacts. The sputtered gold served as an ion-blocking electrode. Data were collected in 12.5 °C increments at temperatures ranging from −100 to 100 °C, since 100 °C is near the upper limit for which the sample cell precludes sample oxidation. The temperature was allowed to stabilize within 0.5 °C of the set temperature for 3 min before data collection. The complex impedance arcs were fit using Novocontrol WinFIT 3.2 software (Novocontrol Technologies GmbH & Co. KG) to determine the resistance (R), which is equal to the real component of the impedance when the imaginary component of the impedance passes through a local minimum. The resistance, the pellet thickness, and electrode area were used to determine the conductivity. Data sets were collected from low temperature to high temperature, and subsequent data recollection at room temperature and then high temperature indicated reproducibility.

2.7. Diffuse Reflectance UV−Vis−NIR Spectroscopy. A Cary 5000 UV−vis−NIR spectrometer was used with $BaSO_4$ (Fisher, 99.92%) as a 100% reflectance standard for the collection of optical diffuse reflectance data for Li_2SnS_3. A Harrick Praying Mantis diffuse reflectance accessory was used to hold the Li_2SnS_3 sample, and scans were performed from 200 to 2500 nm at a rate of 600 nm/min. The percent reflectance data were converted to absorption using the Kubelka−Munk equation.[17]

2.8. Differential Thermal Analysis. A Shimadzu DTA-50 differential thermal analyzer was used with an Al_2O_3 reference for thermal analysis of Li_2SnS_3. The instrument was calibrated using a three-point method with indium, zinc, and gold standards. The reference and sample, of comparable mass, were vacuum-sealed in fused-silica ampules. The ampule containing Li_2SnS_3 was carbon-coated before adding the sample to minimize the reaction of the compound with the ampule at high temperatures. The ampules were heated at a rate of 10 °C/min to 800 °C, held for 1 min, and cooled at 10 °C/min.

2.9. Computer Simulation Methods. Electronic structure calculations were carried out in the framework of density functional theory,[18] using the projector augmented wave (PAW) method[19] as implemented in the Quantum Expresso[20] and abinit[21] packages. The PAW atomic data files were generated using the atompaw code.[22] Geometry and volume optimizations were performed starting with the crystal structures of Li_2SnS_3 and Li_2SnO_3, determined from single-crystal X-ray diffraction in this work and by Kreuzburg et al., respectively.[23] The local density approximation (LDA)[24] was used to treat the exchange and correlation effects. The plane wave expansion of the wave functions was found to be well-converged within the cutoff criterion $|\mathbf{k} + \mathbf{G}| \leq 8$ bohr^{-1} (in terms of the wave vector $\mathbf{k}$ and reciprocal lattice vector $\mathbf{G}$). The $\mathbf{k}$-point integrations were estimated using sampling volumes of 0.005 bohr^{-3} or less. Internal tests estimate the numerical errors for relative energies to be within 0.001 eV/formula unit. The computed lattice parameters, shown in Table S6, are ~2% underestimated (as expected for the LDA functional); however, the relative lattice shape and the fractional atomic coordinates, shown in Tables S7 and S8, are quite close to the experimental values determined by X-ray methods at room temperature. The band structures were constructed with the AbinitBandStructureMaker.py program.[21] The k-points used for plotting the band structure were chosen to be roughly orthogonal to one another in order to sample along x, y, and z axes, rather than using the conventional symmetry points for the Brillouin zone (Figure 2). The **A** point corresponds to the position $[2\pi/(c \sin \beta)]\hat{\mathbf{z}}$, the **Y** point corresponds to the position $(2\pi/b)\hat{\mathbf{y}}$, and **x** corresponds to the position $(2\pi/a)(\hat{\mathbf{x}} - \hat{\mathbf{z}}/\tan \beta)$.

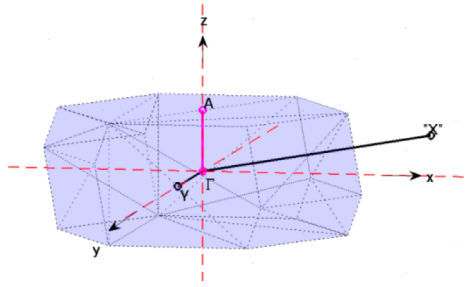

Figure 2. Brillouin zone diagram for the $C2/c$ structure indicating the k-points used to calculate the electronic band structure.

The partial densities of states were based on the charge enclosed within the PAW augmentation sphere of each atom for each state. The heats of formation were estimated by determining the total energies of the solid reference materials, whereas the O reference was determined by fitting as described previously.[25]

3. RESULTS AND DISCUSSION

3.1. Structure. Li_2SnS_3 crystallizes in the $C2/c$ space group with the unit cell parameters shown in Table 1. The structure refinement presented here exhibits better reliability statistics than that reported by Kuhn et al. (Table S5) and has a few significant differences.[26] In contrast to the structure determined by Kuhn et al., our Li(2), Sn(1), and Sn(2) sites are fully occupied, whereas their structure contains mixed site occupation of Li(2)/Sn(3), Li(4)/Sn(1), and Li(5)/Sn(2), as summarized in Table S4. Three crystallographically unique lithium ions, Li(1), Li(2), and Li(3), reside on 8f, 4e, and 4d positions, respectively. Two unique tin ions reside on 4e sites, whereas three unique sulfide ions occupy 8f sites. Our attempts to model disorder on the cation sites resulted in increased R values, and the sites would not tolerate mixed occupancy, evidenced by slightly negative site occupation factors.

Each octahedral lithium and tin ion is coordinated by sulfide ions, yielding a sodium chloride-like structure, as shown in Figure 1b. The electrostatic valence of each octahedral S^{2-} ion

DOI: 10.1021/cm5037524
Chem. Mater. 2015, 27, 189−196

is satisfied via cis coordination to two tin ions, Sn(1) and Sn(2), and coordination to four lithium ions in a seesaw arrangement. All of the Li−S and Sn−S interactions are within typical bonding distances (Tables S2 and S3). The structure can be viewed as $[SnS_3]^{2-}$ layers of honeycomb nets with Sn-vertices (Figure 1c). The Sn^{4+} ions are bridged by S^{2-} ions. With the S atoms removed for clarity, the honeycomb topology of the 6^3 net is apparent in Figure 1d. The honeycomb nets stack in an ABAB fashion. Li(1) and Li(3) reside between the honeycomb layers, and Li(2) is in the center of the six-membered rings.

3.2. Synchrotron X-ray Powder Diffraction (SXRPD). According to Rietveld refinement using SXRPD data, the bulk microcrystalline product is phase-pure and has a sodium chloride-like ($C2/c$) structure. Initial refinements, using the single-crystal diffraction results as a starting model, yielded agreement factors of $\chi^2 = 6.194$, $R_p = 0.1920$, and $wR_p = 0.2323$. However, peak broadening and intensity of some Bragg reflections, especially in the range of $2\theta = 3.5-7°$ ($\lambda = 0.414$ Å), were not sufficiently modeled using this ideal structure. Therefore, we reattempted Rietveld refinement using the structure determined by Kuhn et al.[26] as the starting model, in which the total formula is charge-balanced, two metal sites are occupied by only Li, and three other metal sites exhibit Li/Sn site sharing. The best refinement using this model resulted in a χ^2 of 8.927 ($R_p = 0.2236$ and $wR_p = 0.2789$), which is more unfavorable than the ideal structure described above.

Agreement factors for Rietveld refinement using SXRPD data were improved by introducing occupational disorder, akin to the structure reported by Kuhn et al.[26] but allowing mixed occupation of Li and Sn on all of the cation sites (Table S4). The best agreement factors, $\chi^2 = 3.301$, $R_p = 0.1359$, and $wR_p = 0.1696$, were obtained using this model. This refinement, in which the total occupation of each cation site was constrained to unity, shows that the Sn(1) and Sn(2) sites from our single-crystal structure are ∼50% occupied by Li. The Li(1) and Li(3) sites are shared by ∼30 and <5% Sn, respectively, whereas the Li(2) site is occupied by ∼85% Sn in this $Li_{1.73}Sn_{1.27}S_3$ model that lacks charge balance. While this refinement provides a better fit to the data, the intensity and peak broadening discrepancies are not entirely resolved using this model (Figure S1). Similar cases have been observed in powder diffraction patterns of other NaCl-like A_2BO_3 materials, e.g., Li_2ZrO_3 and Li_2SnO_3.[27] In these cases, introducing A^+/B^{4+} disorder into the honeycomb layers provided a slightly improved fit of the calculated data to the experimental data; however, diffuse intensity streaks in electron diffraction were attributed to stacking faults along the c axis.[28] Likewise, the polycrystalline sample of Li_2SnS_3 is expected to contain stacking faults, as the nonuniform broadening of Bragg reflections is a major indicator.

While the single crystal selected for characterization does, in fact, possess the ideal structure, it is apparent that structural variations occur throughout the polycrystalline powder of the same sample. In addition to the SXRPD data, this observation of structural variations was evident in our single-crystal X-ray diffraction investigation. For numerous specimens, the X-ray diffraction data appeared to be not of single crystals due to significant streaking of reflections. In addition to the perfect structure detailed in Table 1, one other data set yielded a reasonable structure model using single-crystal X-ray diffraction. For this structure, mixed occupations similar to those reported by Kuhn[26] were observed; two of the lithium sites are fully occupied, whereas the Li/Sn occupation for the other metal sites is ∼0.08/0.92, 0.18/0.82, and 0.77/0.23. Fully occupied lithium and tin sites resulted in an unstable refinement for this particular data set, but mixed occupation yielded $R_1[I > 2\sigma(I)] = 0.0467$, $R_2[I > 2\sigma(I)] = 0.1319$, R_1(all data) = 0.0532, and R_2(all data) = 0.1406.

3.3. ^{119}Sn Mössbauer Spectroscopy. The ^{119}Sn Mössbauer spectrum of Li_2SnS_3 exhibits an isomer shift (IS, relative to SnO_2) of ∼1.00(2) mm/s, which is characteristic of octahedral Sn^{4+} ions (Figure 3). This result is comparable to that of the sodium chloride-like Na_2SnS_3, which has an IS of 1.02 mm/s that is attributed to SnS_6 octahedra.[29] The ^{119}Sn Mössbauer spectra of some other thiostannates that contain octahedral Sn^{4+} ions are also comparable, for example, Sn_2S_3 (IS = 1.10−1.15 mm/s)[30] and SnS_2 (IS = 1.06−1.30 mm/s).[30a,31,32] Octahedral Sn^{4+} ions in other sulfides, such as $Sn_5Sb_2S_9$, $PbSnS_3$, and $In_2Sn_3S_7$, give rise to IS values of 1.10−1.19 mm/s.[29,30c,d]

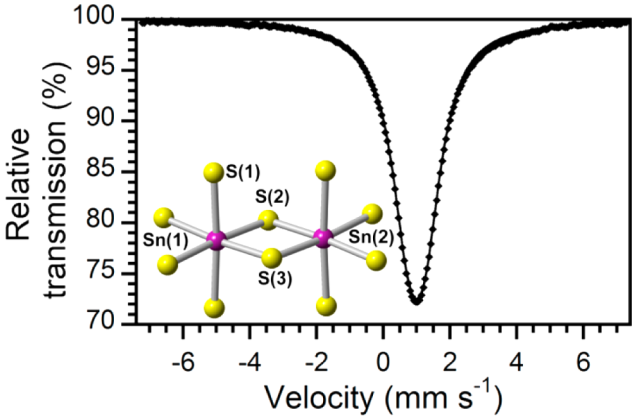

Figure 3. ^{119}Sn Mössbauer spectrum of Li_2SnS_3 recorded at 80 K. The collected data are plotted with diamonds (♦), overlapped by the one-component fit (line). Shown in the bottom left is a piece of the $[SnS_3]^{2-}$ layer to display the coordination environments of Sn(1) and Sn(2).

In contrast, divalent tin ions in SnS and Sn_2S_3 give rise to much higher IS values of 3.2−3.5 mm/s,[30a,b,33] and octahedral Sn^{2+} ions yield an IS value of 3.3 mm/s in $SnBi_2Te_4$.[34] Other examples of Sn^{2+} ions include those with square-based pyramidal and bicapped trigonal prismatic geometries, as found in $GeSnS_3$ (IS = 3.5 mm/s) and $In_2Sn_3S_7$ (IS = 3.82 mm/s), respectively.[30d,35] Sn^{4+} ions in SnS_4 tetrahedra yield IS values that are slightly higher than that of Li_2SnS_3, ranging from 1.17 to 1.48 mm/s (e.g., Li_2FeSnS_4, Na_4SnS_4, Tl_2SnS_3, etc.)[29,36]

The one-component fit, assuming Lorentzian line shapes, for the spectrum is in good agreement with the crystal structure, in which the environments of the two crystallographically unique tin ions are virtually identical. However, the case in which lithium and tin participate in site sharing on several nonequivalent crystallographic sites that lends subtle environmental variations cannot be ruled out by this data. While either case is difficult to confirm with this zero-external-field spectrum, the one-component fit exhibits a quadrupole splitting (ΔE_Q) of 0.49(2) mm/s and a half-line width ($\Gamma/2$) of 0.63(2) mm/s, which is broader than the 23.9 keV ^{119}Sn transition natural half-line width.[33a] An alternative fit using a Gaussian spread of ΔE_Q values gave an identical IS

DOI: 10.1021/cm5037524
Chem. Mater. 2015, 27, 189−196

(1.00(2) mm/s) value and slightly reduced Γ/2 (0.61(2) mm/s) and ΔE_Q (0.45(2) mm/s) values relative to the nondistributed case. However, the resulting total ΔE_Q spread of 0.32(2) mm/s gave only a marginal decrease (3.7%) of the χ^2 value of the fit. The ΔE_Q of Li_2SnS_3 (0.45(2) mm/s) is comparable to the ΔE_Q = 0.4 mm/s for Na_2SnS_3.[29] This line broadening could potentially be due to contributions from Sn^{4+} ions with slightly different environments.

3.4. Lithium Ion Conductivity. The conductivity of Li_2SnS_3 was determined using frequency-dependent complex impedance, $\hat{Z}(f) = Z'(f) + iZ''(f)$. The semicircle at high frequency and the low-frequency spike observed in the complex impedance plots are characteristic of a pure ion conductor (Figure 4). The semicircle is attributed to bulk conductivity,

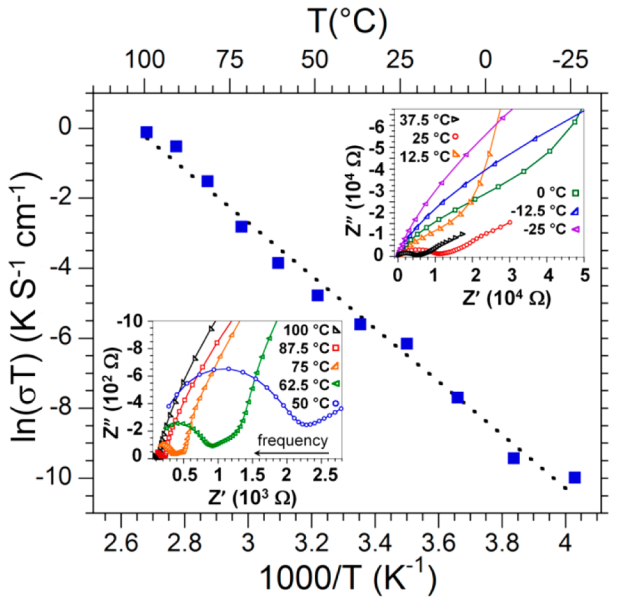

Figure 4. Lithium ion conductivity of Li_2SnS_3. The Arrhenius plot, with a linear fit of R^2 = 0.997, represents the bulk conductivities extracted from complex impedance plots (insets) of data collected from low to high temperature.

whereas the spike is a product of space-charge polarization effects from the accumulation of Li^+ ions at the Au electrodes on the pellet. The real part of conductivity, $\sigma'(f) = t/A(Z'(f)/([Z'(f)]^2 + [Z''(f)]^2)$, where t is pellet thickness and A is the area of the electrode, is obtained from the circuit resistance (R) that is equal to the real impedance (Z') when the imaginary impedance (Z'') is at a local minimum at low frequencies (i.e., $R = Z'$ when $Z'' \sim 0$; $\sigma_{dc} = t/[R{\cdot}A]$).

The lithium ion conductivity of Li_2SnS_3, $\sigma_{100°C} = 1.6 \times 10^{-3}$ S/cm and $\sigma_{25°C} = 1.5 \times 10^{-5}$ S/cm, is a vast improvement compared to the closely related polycrystalline, ternary thio-LISICONs: Li_2GeS_3 ($\sigma_{125°C} = 9.7 \times 10^{-9}$ S/cm), Li_5GaS_4 ($\sigma_{100\ °C} = 5.1 \times 10^{-8}$ S/cm), and Li_4GeS_4 ($\sigma_{25°C} = 2.0 \times 10^{-7}$ S/cm).[2k] The room-temperature conductivity of Li_2SnS_3 is 2 orders of magnitude higher than the related ternary chalcogenide, $Li_4Sn_2Se_6$ ($\sigma_{25°C} = 2 \times 10^{-7}$ S/cm).[37] Interestingly, the Li_2SnSe_3 analogue crystallizes in the monoclinic spacegroup *Cc* and is composed of $\{[SnSe_3]^{2-}\}_n$ chains of corner-sharing $SnSe_4$ tetrahedra.[37] Kaib et al. reported the lithium ion conductivity for the $Li_4Sn_2Se_6$ compound that is accessed by drying $Li_4[Sn_2Se_6]{\cdot}14H_2O$ that crystallizes in the space group $P\bar{1}$ and is composed of dimeric $[Sn_2Se_6]^{4-}$ anions and hydrated lithium atoms.[37] Li_2SnSe_3 (*Cc*) and dried $Li_4[Sn_2Se_6]{\cdot}14H_2O$ differ due to interruptions in the $\{[SnSe_3]^{2-}\}_n$ chains.[37] Another ternary chalcogenide, Li_4SnSe_4, has an ion conductivity at 100 °C ($\sigma_{100°C} = 9 \times 10^{-4}$ S/cm) that is ∼2× lower than Li_2SnS_3.[37] The $\sigma_{100°C}$ of Li_2SnS_3 is ∼2× lower than that of Li_4SnS_4 ($\sigma_{100°C} = 3 \times 10^{-3}$ S/cm), which exhibits conductivity that is among the highest in ternary solids,[38] as well as conductivity that is on par with that of Li_3N that is accessed at much higher temperatures.[2a]

The conductivity values reported here for a pellet of Li_2SnS_3 with 56% compactness are expected to increase considerably as the pellet density approaches the theoretical density. For example, a pellet of SD-Li_2PO_2N with 78% compactness shows conductivity that is more than 2 orders of magnitude higher than the conductivity of a pellet with 55% compactness.[39] While the conductivity values reported here are on par with leading solid electrolytes and greater than those of related polycrystalline phases, the Li^+ ion conductivity is likely to increase at least an order of magnitude or more in Li_2SnS_3 pellets with higher densities.

The ionic conductivity of Li_2SnS_3 follows the Arrhenius relationship within the temperature range measured. Thus, the activation energy for Li^+ ion conduction (ΔE_A) was calculated using $\sigma_{dc}(T) = \sigma_o/T \exp(-\Delta E_A/RT)$, where σ_{dc} is the dc ionic conductivity, σ_o is a pre-exponential factor, T is the temperature, and R is the gas constant. The ΔE_A for Li_2SnS_3 is 0.59 eV, which is comparable to commercial LiPON and the crystalline Li_2PO_2N.[39,40]

3.5. Electronic Structure. *3.5.1. Calculations.* As lithium sulfides with high stability are gaining precedence in the search for new solid-state electrolytes, the electronic structure and thermodynamic stability of Li_2SnS_3 are investigated and compared to those of the isostructural oxide, Li_2SnO_3. The calculated electronic band structures for Li_2SnS_3 and Li_2SnO_3 are shown in Figure 5. Li_2SnS_3 is calculated to be an indirect bandgap semiconductor with a bandgap (E_g) of 1.25 eV. However, since the direct gaps at the **Y** and **X** points have the same value within the calculational accuracy, we expect that the optical properties of Li_2SnS_3 should behave as a direct gap material. As expected for DFT calculations, the calculated E_g is underestimated compared to the experimentally determined optical E_g of 2.38 eV (521 nm) that is discussed later in Section 3.5.2.

The calculated band structure of Li_2SnO_3 also shows an indirect gap from the **Y** point at the valence band maximum to the Γ point at the conduction band minimum, with a calculated value of 3.55 eV. While we expect that this calculated E_g is an underestimation, the fact that the more ionic oxide analogue is expected to have a wider bandgap than the sulfide is correctly modeled. To the best of our knowledge the exact value for the optical absorption edge of Li_2SnO_3 has not been reported; however, we can estimate the value to be ∼5 eV (250 nm) from the optical diffuse reflectance spectrum reported by Hosogi et al.[41]

As illustrated in Figure 6, the partial density of states, based on the charge within the augmentation sphere of each atom, plots for Li_2SnS_3 and Li_2SnO_3 are qualitatively similar. The Sn 4d states and the anion valence s states lie deep in the valence band and are not shown in this plot. For both compounds, the densities of states below the Fermi level are dominated by contributions from the anion p states. The lower energy states are characterized by bonding hybrid states formed from the anion p and Sn 5s and 5p orbitals. In both compounds, the

DOI: 10.1021/cm5037524
Chem. Mater. 2015, 27, 189−196

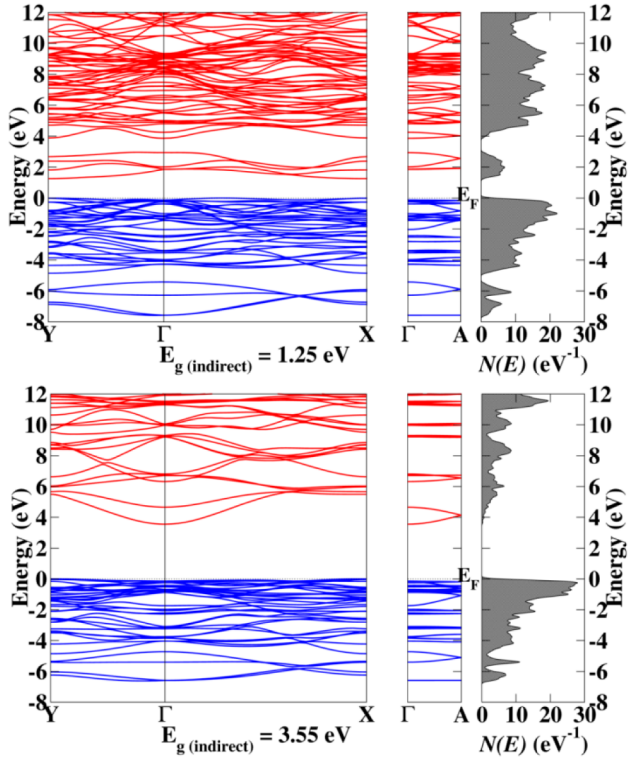

Figure 5. Electronic band structure and the corresponding total density of states for Li_2SnS_3 (top) and Li_2SnO_3 (bottom). The top of the valence is denoted as the dotted line and labeled E_F.

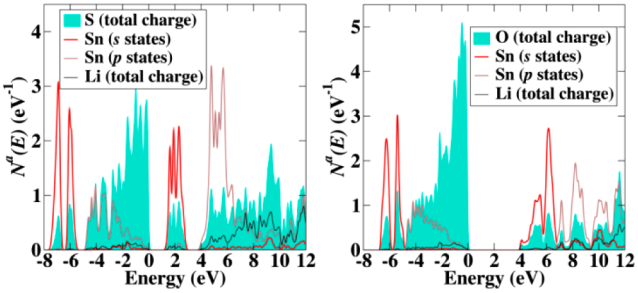

Figure 6. Partial density of states for Li_2SnS_3 (left) and Li_2SnO_3 (right) indicating the total contributions from Li and the S or O anions as well as the s and p decomposed contributions from Sn.

bottom of the conduction band is characterized by the antibonding hybrid states formed from the anion p and Sn 5s (at the bottom of the band) and 5p orbitals.

The participation of lithium cations in covalent interactions is minimal; thus, there are no states in the valence band that predominately arise from lithium. The major donations from the lithium ions arise in the conduction band states at energies greater than 6 eV. Quantitatively, the much smaller bandgap of Li_2SnS_3 is consistent with the general trend for this substitution. From the viewpoint of the partial densities of states diagrams, the larger bandgap for Li2SnO3 is consistent with its larger bonding−antibonding energy splitting for O 2p−Sn 5s hybrid states.

3.5.2. Optical Bandgap. To estimate the bandgap of Li_2SnS_3 (Figure 7) using diffuse reflectance UV−vis−NIR spectroscopy, the Urbach tail energy is first determined so that it can be excluded from the absorption edge. Urbach tailing near the absorption edge primarily arises from defects and disorder

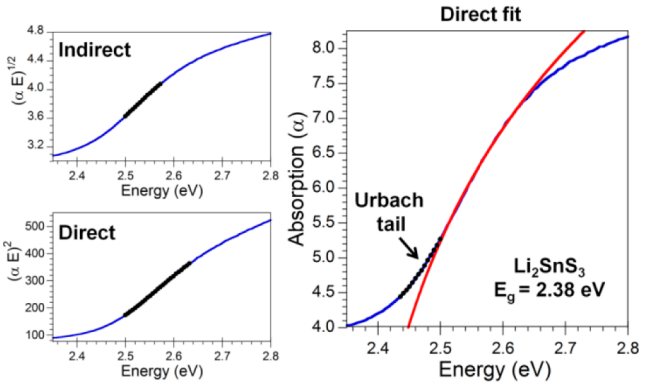

Figure 7. Optical diffuse reflectance UV−vis−NIR data for Li_2SnS_3. (Left) The data are fit using an indirect function (top) and a direct function (bottom) with linear regions depicted in black. (Right) The collected data (blue) is fit with the function for direct gap semiconductors (red) while disregarding the Urbach tail (black).

within the structure, which cause the density of states near the valence band edge and the conduction band edge to develop tails that extend into the bandgap region. The Urbach energy is attained by fitting $\alpha = A \exp[(E - E_g)/E_u]$, in which A is a constant, E is the photon energy, E_g is the bandgap energy, and E_u is the Urbach energy, to a portion of the optical data that is selected as a linear region in a plot of the logarithm of absorption versus photon energy.[42]

The nature of the bandgap (i.e. direct or indirect) is determined by considering the absorption edge at energies above the Urbach tail. A sharp absorption edge is indicative of a direct bandgap, whereas a gradual onset of absorption is characteristic of an indirect bandgap.[43] The absorption edges for direct and indirect bandgaps can be fit with the functions $\alpha = A\cdot(E - E_g)^{1/2}/E$ and $\alpha = A\cdot(E - E_g)^2/E$, respectively. Accordingly, a direct gap material yields a longer linear region in a $(\alpha E)^2$ vs E plot, whereas an indirect gap is characterized by a longer linear region in a $(\alpha E)^{1/2}$ vs E plot. Since the optical data above the Urbach tail has a wider linear region in the $(\alpha E)^2$ vs E plot, as shown in Figure 7, Li_2SnS_3 is assigned a direct bandgap. Accordingly, fitting the optical data (at energies above the Urbach tail) with the direct gap function yields a bandgap of 2.382(7) eV for Li_2SnS_3.

3.6. Li^+ Ion Migration. While a complete study of the Li^+ ion migration is beyond the scope of the present study, we have some preliminary computational results for simulations performed on supercells with the dimensions of 2*a*, *b*, and *c* of the conventional lattice. For Li_2SnO_3, we found that it is energetically favorable to create vacancies at the 4e (Li(2)) sites compared with the formation at the 8f (Li(1)) or 4d (Li(3)) sites by 0.1 eV. In contrast, for Li_2SnS_3, we found that it is energetically unfavorable to create vacancies at the 4e (Li(2)) sites compared with the vacancy formation at the 8f (Li(1)) or 4d (Li(3)) sites by −0.3 eV.

Interestingly, these results indicate lower activation barriers for forming lithium ion vacancies within the lithium sulfide layers, which are between the honeycomb-like $[SnS_3]^{2-}$ layers that are perpendicular to the *c* axis as depicted in Figure 1, than for forming lithium ion vacancies within the $[SnS_3]^{2-}$ layers in the center of the six-membered rings. While the opposite case is expected for Li_2SnO_3, the six-membered rings within the $[SnO_3]^{2-}$ honeycomb-like layers are smaller than those in the $[SnS_3]^{2-}$ analogues. However, the spacing between the ABAB $[SnS_3]^{2-}$ layers in Li_2SnS_3 is wider than that between the

DOI: 10.1021/cm5037524
Chem. Mater. 2015, 27, 189−196

$[SnO_3]^{2-}$ layers in Li_2SnO_3 and may give rise to more accessible lithium ion diffusion. For instance, the distance from a Sn site in an A-layer to an analogous A-layer Sn site is 12.405 Å in the Li_2SnS_3 structure, whereas the corresponding distance in the structure of Li_2SnO_3 is 10.032 Å. We propose that Li(1) and Li(3) are the likely origins of Li^+ ion mobility in Li_2SnS_3, as opposed to Li(2) that resides in the center of the six-membered rings of the honeycomb-like layers.

3.7. Stability. Li_2SnS_3 is stable in air under ambient conditions (Figure S2), and the DTA diagram for Li_2SnS_3 indicates that the sample undergoes one major thermal event at 756.3 °C upon heating that is attributed to melting and one at 747.9 °C while cooling that is considered to arise from the recrystallization (Figure 8). The thermal stability of Li_2SnS_3 is comparable to that of $Li_{10}SnP_2S_{12}$, which begins to decompose at temperatures over 700 °C.[6]

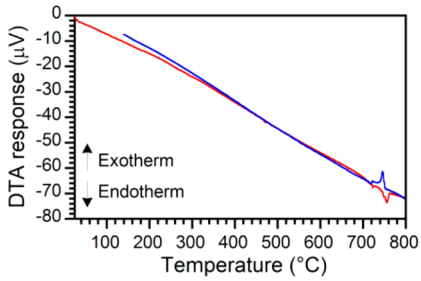

Figure 8. Differential thermal analysis diagram for the heating/cooling cycle for Li_2SnS_3. The heating and cooling portions of the cycle are depicted in red and blue, respectively.

In order to evaluate the chemical stability of Li_2SnS_3 and Li_2SnO_3, we estimated the heats of formation (at 0 K) relative to the binary decomposition products in standard states (Table 2). When available, experimentally determined heats of formation were compared to the calculations, and reasonable agreement was found. All of the scenarios for decomposition based on these products were considered, and the results suggest that both Li_2SnS_3 and Li_2SnO_3 are stable relative to decomposition products. For example, the calculations for Li_2SnS_3 suggest that it is slightly stable relative to decomposition into Li_2S and SnS_2 in the sense that

Table 2. Heats of Formation of Li_2SnS_3 and Li_2SnO_3 and Possible Decomposition Products in Units of eV/Formula Unit[a]

compound	space group	calculated ΔH (eV)	measured ΔH (eV)
Li_2SnS_3	$C2/c$ (#15)	−5.89	
Li_2SnO_3	$C2/c$ (#15)	−12.70	
Li_2O	$Fm\bar{3}m$ (#225)	−6.19	−6.20
Li_2O_2	$P6_3/mmc$ (#194)	−6.52	−6.57
Li_2S	$Fm\bar{3}m$ (#225)	−4.30	−4.57
Li_2S_2	$P6_3/mmc$ (#194)	−4.09	
SnS	$Pnma$ (#62)	−1.07	−1.036
SnS_2	$P\bar{3}m1$ (#164)	−1.32	−1.592
Sn_2S_3	$Pnma$ (#62)	−2.35	−2.732
SnO	$P4/nmn$ (#129)	−2.95	−2.909
SnO_2	$P6_3mc$ (#186)	−5.79	−5.987

[a]The measured values were taken from NIST[44] and the CRC handbook.[45]

$$\Delta H(Li_2SnS_3) = \Delta H(Li_2S) + \Delta H(SnS_2) - 0.27\ \text{eV}. \quad (1)$$

This is the scenario in which the difference in heats of formation is the smallest, and this difference is greater than the expected calculation error. For the oxide compound we find that

$$\Delta H(Li_2SnO_3) = \Delta H(Li_2O) + \Delta H(SnO_2) - 0.72\ \text{eV}. \quad (2)$$

Li_2SnS_3 is even more stable with respect to decomposition into Li_2S_2 and SnS in the sense that

$$\Delta H(Li_2SnS_3) = \Delta H(Li_2S_2) + \Delta H(SnS) - 0.73\ \text{eV}. \quad (3)$$

Similarly, the oxide also shows similar increasing stability with respect to decomposition into Li_2O_2 and SnO as shown in the equation

$$\Delta H(Li_2SnO_3) = \Delta H(Li_2O_2) + \Delta H(SnO) - 3.23\ \text{eV}. \quad (4)$$

4. CONCLUSIONS

Achieving materials that simultaneously exhibit exceptional Li^+ ion conductivity and stability is key to the emergence of next-generation batteries. The fast ion conductor, Li_2SnS_3, exhibits thermal stability up to ∼750 °C and environmental stability as well as calculated stability with respect to decomposition products. The lithium ion conductivity in Li_2SnS_3 (1.6×10^{-3} S/cm at 100 °C) rivals some of the most promising solid-state electrolytes, such as $Li_{10}SnP_2S_{12}$ with a conductivity of $\sim 4 \times 10^{-3}$ S/cm at 27 °C in an annealed pellet.[6] The conductivity is expected to improve substantially with higher pellet density, and these results for Li_2SnS_3 are especially promising considering that the pellet analyzed was only ∼56% of the theoretical density. While the crystal selected for single-crystal X-ray diffraction showed the ideal structure, structural imperfections are present in the polycrystalline powder according to synchrotron X-ray powder diffraction. On the basis of first-principles calculations, we have proposed that the origin of the fast ion conductivity in Li_2SnS_3 arises from the mobility of Li(1) and Li(3) that reside in the lithium sulfide layers between the honeycomb-like $[SnS_3]^{2-}$ layers. The ion conductivity and stability deem Li_2SnS_3 as a potential component in innovative solid-state batteries.

■ ASSOCIATED CONTENT

Supporting Information

Details regarding single-crystal X-ray diffraction (CIF file), synchrotron X-ray powder diffraction and Rietveld refinement, electronic structure, and laboratory-grade X-ray powder diffraction. This material is available free of charge via the Internet at http://pubs.acs.org.

■ AUTHOR INFORMATION

Corresponding Author

*E-mail: aitkenj@duq.edu.

Notes

The authors declare no competing financial interest.

■ ACKNOWLEDGMENTS

This work was supported by the National Science Foundation (NSF) under grant nos. DMR-0645304 (CAREER Award) and DMR-1201729. Use of the Advanced Photon Source at Argonne National Laboratory was supported by the U.S.

DOI: 10.1021/cm5037524
Chem. Mater. 2015, 27, 189−196

Department of Energy, Office of Science, Office of Basic Energy Sciences, under contract no. DE-AC02-06CH11357. The work by NAWH was support by NSF grant no. DMR-1105485. J.H.M. thanks the NSF for support through a supplemental ROA award and an REU program under grant nos. DMR-0935302 and CHE-1263279, respectively. S. W. Martin was supported by NSF grant no. DMR-1304977. We additionally thank Brian Toby for valuable discussions.

REFERENCES

(1) Kamaya, N.; Homma, K.; Yamakawa, Y.; Hirayama, M.; Kanno, R.; Yonemura, M.; Kamiyama, T.; Kato, Y.; Hama, S.; Kawamoto, K.; Mitsui, A. *Nat. Mater.* **2011**, *10*, 682−686.

(2) (a) Alpen, U. V.; Pabenau, A.; Talat, G. H. *Appl. Phys. Lett.* **1977**, *30*, 621−623. (b) Edman, L.; Ferry, A.; Doeff, M. M. *J. Mater. Res.* **2000**, *15*, 1950−1954. (c) Croce, F.; Appetecchi, G. B.; Persi, L.; Scrosati, B. *Nature* **1998**, *394*, 456−458. (d) Kondo, S.; Takada, K.; Yamamura, Y. *Solid State Ionics* **1992**, *53*, 1183−1186. (e) Takada, K.; Aotani, N.; Kondo, S. *J. Power Sources* **1993**, *43*, 135−141. (f) Inaguma, Y.; Liquan, C.; Itoh, M.; Nakamura, T. *Solid State Commun.* **1993**, *86*, 689−693. (g) Mizuno, F.; Hayashi, A.; Tadanaga, K.; Tatsumisago, M. *Adv. Mater.* **2005**, *17*, 918−921. (h) Hayashi, A.; Minami, K.; Mizuno, F.; Tatsumisago, M. *J. Mater. Sci.* **2008**, *43*, 1885−1889. (i) Hong, H. Y.-P. *Mater. Res. Bull.* **1978**, *12*, 117−124. (j) Bruce, P. G.; West, A. R. *J. Solid State Chem.* **1982**, *44*, 354−365. (k) Kanno, R.; Hata, T.; Kawamoto, Y.; Irie, M. *Solid State Ionics* **2000**, *130*, 97−104. (l) Kanno, R.; Murayama, M. *J. Electrochem. Soc.* **2001**, *148*, A742−A746. (m) Liu, Z.; Fu, W.; Payzant, E. A.; Yu, X.; Wu, Z.; Dudney, N. J.; Kiggans, J.; Hong, K.; Rondinone, A. J.; Liang, C. *J. Am. Chem. Soc.* **2013**, *135*, 975−978.

(3) Kuhn, A.; Duppel, V.; Lotsch, B. V. *Energy Environ. Sci.* **2013**, *6*, 3548−3552.

(4) Stallworth, P. E.; Fontanella, J. J.; Wintersgill, M. C.; Scheidler, C. D.; Immel, J. J.; Greenbaum, S. G.; Gozds, A. S. *J. Power Sources* **1999**, *81*−*82*, 739−747.

(5) Kuhn, A.; Gerbig, O.; Zhu, C.; Falkenberg, F.; Maier, J.; Lotsch, B. V. *Phys. Chem. Chem. Phys.* **2014**, *16*, 14669−14674.

(6) Bron, P.; Johansson, S.; Zick, K.; auf der Günne, J. S.; Dehnen, S.; Roling, B. *J. Am. Chem. Soc.* **2013**, *135*, 15694−15697.

(7) Sakuda, A.; Hayashi, A.; Tatsumisago, M. *Sci. Rep.* **2013**, *3*, 2261.

(8) Sahu, G.; Lin, Z.; Li, J.; Liu, Z.; Dudney, N.; Liang, C. *Energy Environ. Sci.* **2014**, *7*, 1053−1058.

(9) *SAINT and SADABS*; Bruker Analytical X-ray Systems, Inc.: Madison, WI, 2005.

(10) Sheldrick, G. M. *Acta Crystallogr., Sect. A* **2007**, *64*, 112−122.

(11) *SHELXTX-PC*, release 6.14; Bruker AXS: Madison, WI, 2007.

(12) Wang, J.; Toby, B. H.; Lee, P. L.; Ribaud, L.; Antao, S.; Kurtz, C.; Ramanathan, M.; Von Dreele, R. B.; Beno, M. A. *Rev. Sci. Instrum.* **2008**, *79*, 085105.

(13) Lee, P. L.; Shu, D.; Ramanathan, M.; Preissner, C.; Wang, J.; Beno, M. A.; Von Dreele, R. B.; Lynn, R.; Kurtz, C.; Antao, S. M.; Jiao, X.; Toby, B. H. *J. Synchrotron Radiat.* **2008**, *15*, 427−432.

(14) Dalesio, L. R.; Hill, J. O.; Kraimer, M.; Lewis, S.; Murray, D.; Hunt, S.; Watson, W.; Clausen, M.; Dalesio, J. *Nucl. Instrum. Methods Phys. Res., Sect. A* **1994**, *352*, 179−184.

(15) (a) Larson, A. C.; Von Dreele, R. B. *Los Alamos Natl. Lab., [Rep.] LA (U.S.)* **1994**, 86−748. (b) Toby, B. H. *J. Appl. Crystallogr.* **2001**, *34*, 210−213.

(16) Douvalis, A. P.; Polymeros, A.; Bakas, T. *J. Phys.: Conf. Ser.* **2010**, *217*, 012014.

(17) Kubelka, P.; Munk, F. *Z. Technol. Phys.* **1931**, *12*, 593−601.

(18) (a) Hohenberg, P.; Kohn, W. *Phys. Rev.* **1964**, *136*, B864. (b) Kohn, W.; Sham, L. J. *Phys. Rev.* **1965**, *140*, A1133.

(19) Blöchl, P. E. *Phys. Rev. B* **1994**, *50*, 17953.

(20) Giannozzi, P.; Baroni, S.; Bonini, N.; Calandra, M.; Car, R. *J. Phys.: Condens. Matter* **2009**, 395502.

(21) Gonze, X.; Amadon, B.; Anglade, P.-M.; Beuken, J.-M. *Comput. Phys. Commun.* **2009**, *180*, 2582−2615.

(22) Tackett, A. R.; Holzwarth, N. A. W.; Matthews, G. E. *Comput. Phys. Commun.* **2001**, *135*, 348−376.

(23) Kreuzburg, G.; Stewner, F.; Hoppe, R. *Z. Anorg. Allg. Chem.* **1971**, *379*, 242−254.

(24) Perdew, J. P.; Wang, Y. *Phys. Rev. B* **1992**, *45*, 13244.

(25) Lepley, N. D.; Holzwarth, N. A. W.; Du, Y. A. *Phys. Rev. B* **2013**, *88*, 104103.

(26) Kuhn, A.; Holzmann, T.; Nuss, J.; Lotsch, B. V. *J. Mater. Chem. A* **2014**, *2*, 6100−6106.

(27) Hodeau, J. L.; Marezio, M.; Santoro, A.; Roth, R. S. *J. Solid State Chem.* **1982**, *45*, 170−179.

(28) (a) Tarakina, N. V.; Denisova, T. A.; Maksimova, L. G.; Baklanova, Y. V.; Tyutyunnik, A. P.; Berger, I. F.; Zubkov, V. G.; van Tendeloo, G. *Z. Kristallogr.* **2009**, *30*, 375−380. (b) Panin, R. V.; Khasanova, N. R.; Abakumov, A. M.; Antipov, E. V.; Van Tendeloo, G.; Schnelle, W. *J. Solid State Chem.* **2007**, *180*, 1566−1574. (c) Breger, J.; Jiang, M.; Dupre, N.; Meng, Y. S.; Shao-Horn, Y.; Ceder, G.; Grey, C. P. *J. Solid State Chem.* **2005**, *178*, 2575−2585.

(29) Greatrex, R.; Greenwood, N. N.; Ribes, M. *J. Chem. Soc., Dalton Trans.* **1976**, *6*, 500−504.

(30) (a) Ichiba, S.; Katada, M.; Negita, H. *Chem. Lett.* **1974**, *3*, 979−982. (b) Amthauer, G.; Fenner, J.; Hafner, S.; Holzapfel, W. B.; Keller, R. *J. Chem. Phys.* **1970**, *70*, 4837−4842. (c) Jumas, J. C.; Olivier-Fourcade, J.; Ribes, M.; Philippot, E.; Maurin, M. *Bull. Soc. Chim. Fr.* **1980**, *37*, 11. (d) Adenis, C.; Olivier-Fourcade, J.; Jumas, J. C.; Philippot, E. *Rev. Chim. Miner.* **1986**, *23*, 735.

(31) O'Hare, D.; Jaegermann, W.; Williamson, D. L.; Ohuchi, F. S.; Parkinson, B. A. *Inorg. Chem.* **1988**, *27*, 1537−1542.

(32) Stevens, J. G.; Goforth, M. A. *^{119}Sn Mössbauer Spectroscopy*; Mössbauer Effect Data Center: Asheville, NC, 1993.

(33) (a) Greenwood, N. N.; Gibb, T. C. *Mössbauer Spectroscopy*; Chapman and Hall Ltd: London, 1971. (b) Donaldson, J. D.; Senior, B. J. *J. Inorg. Nucl. Chem.* **1969**, *31*, 881−884.

(34) Ledda, F.; Muntoni, C.; Serci, S. *Chem. Phys. Lett.* **1987**, *134*, 545−548.

(35) von Feltz, A.; Schlenzig, E.; Arnold, D. *Z. Anorg. Allg. Chem.* **1974**, *403*, 243−250.

(36) (a) Brant, J. A.; dela Cruz, C.; Yao, J.; Douvalis, A. P.; Bakas, T.; Sorescu, M.; Aitken, J. A. *Inorg. Chem.* **2014**, *53*, 12265−12274. (b) Di Benedetto, F.; Bernardini, G. P.; Borrini, D.; Lottermoser, W.; Tippelt, G.; Amthauer, G. *Phys. Chem. Miner.* **2005**, *31*, 683−690. (c) Eibschütz, M.; Hermon, E.; Shtrikman, S. *J. Phys. Chem. Solids* **1967**, *28*, 1633−1636. (d) Yamanaka, T.; Kato, A. *Am. Mineral.* **1976**, 260−265. (e) Ibanez, A.; Jumas, J. C.; Philippot, E.; Ajavon, A. L.; Eholie, R. *Rev. Chim. Miner.* **1986**, *23*, 281−289.

(37) Kaib, T.; Bron, P.; Haddadpour, S.; Mayrhofer, L.; Pastewka, L.; Järvi, T. T.; Moseler, M.; Roling, B.; Dehnen, S. *Chem. Mater.* **2013**, *25*, 2961−2969.

(38) Kaib, T.; Haddadpour, S.; Kapitein, M.; Bron, P.; Schroder, C.; Eckert, H.; Roling, B.; Dehnen, S. *Chem. Mater.* **2012**, *24*, 2211−2219.

(39) Senevirathne, K.; Day, C. S.; Gross, M. D.; Lachgar, A.; Holzwarth, N. A. W. *Solid State Ionics* **2013**, *233*, 95−101.

(40) Wang, B.; Kwak, B. S.; Sales, B. C.; Bates, J. B. *J. Non-Cryst. Solids* **1995**, *183*, 297−306.

(41) Hosogi, Y.; Kato, H.; Kudo, A. *J. Mater. Chem.* **2008**, *18*, 647−653.

(42) Urbach, F. *Phys. Rev.* **1953**, *92*, 1324.

(43) Pankove, J. I. *Optical Properties in Semiconductors*; Dover Publications: New York, 1971.

(44) Chase, M. W., Jr.; Davies, C. A.; Downey, J. R., Jr.; Frurip, D. J.; McDonald, R. A.; Syverud, A. N. *NIST JANAF Thermochemical Tables 1985*; National Institute of Standards and Technology: Gaithersburg, MD, 1986.

(45) *CRC Handbook of Chemistry and Physics*, 92nd ed.; Haynes, W. M., Ed.; CRC Press: Boca Raton, FL, 2011.

DOI: 10.1021/cm5037524
Chem. Mater. 2015, 27, 189−196